

Microtexture and Grain Boundaries in Freestanding CVD Diamond Films: Growth and Twinning Mechanisms

By Tao Liu,* Dierk Raabe,* Weimin Mao, and Stefan Zaefferer

Three groups of free-standing chemical vapor deposition (CVD) diamond films formed with variations in substrate temperature, methane concentration, and film thickness are analyzed using high-resolution electron back-scattering diffraction. Primarily {001}, {110}, and {111} fiber textures are observed. In addition, corresponding primary and higher order twinning components are found. As interfaces, high angle, low angle, primary twin, and secondary twin boundaries are observed. A growth and a twinning model are proposed based on the sp^3 hybridization of the bond in the CH_4 molecule that is used as the deposition medium.

1. Introduction

Because of its extreme physical properties (e.g., highest hardness and thermal conductivity, wide band gap (~ 5.5 eV), and broad optical transparency), diamond is an important functional material.^[1–5] Since many of its properties, such as heat and electrical conductivity, optical behavior, and mechanical properties, depend on the crystallographic direction, it is important to understand the influence of the deposition parameters on the evolution of texture and microstructure.^[6–13] For instance, in the field of mechanical properties and wear it has been observed that [100]-textured films reveal lower roughness and higher wear resistance than other crystallographic directions, so that [100]-textured diamond films are of interest in tribology.^[11] $\langle 100 \rangle$ -textured films are also optimal for heat transport as the heat conductivity in the $\langle 100 \rangle$ direction exceeds that in the $\langle 111 \rangle$ and $\langle 110 \rangle$ directions.^[7,8] Highly oriented {100} grains were reported to be beneficial for electrical properties.^[9] {111} surfaces of diamond films reveal a negative electron affinity, i.e., they emit electrons in the presence of sufficiently large electrical fields.^[14] For optical applications, the properties of {001} films are superior to those of

{111}-oriented ones in terms of the refractive index and extinction coefficient.^[9]

Various techniques have been used to study diamond film textures, namely, X-ray Bragg diffraction (XRD) for statistical texture analysis,^[15,16] transmission electron microscopy (TEM) for defect studies,^[17,18] and electron back-scattering diffraction (EBSD) for microtexture and twinning analysis.^[16,19,20] However, a systematic investigation of the microtexture of diamond films, including parameter variations of substrate temperature, methane concentration, and film thickness, has not been conducted yet. In

this work we investigate the texture and interfaces as a function of the deposition parameters during CVD (chemical vapor deposition) diamond film growth by means of a high-resolution (HR)-EBSD technique to understand the mechanisms that dominate the formation of thin film diamond textures.

2. Experimental

To date, most CVD techniques for diamond films have in common that the precursor molecules are activated either thermally (e.g., hot filament) or by plasma (e.g., direct current CVD and microwave CVD).^[2] Each of these techniques has its benefits and drawbacks. For instance, high growth rates are usually limited to very small deposition areas smaller than 1 cm^2 , and generally, there is an inverse relationship between film quality and deposition rate. Nevertheless, the direct current CVD technique provides a good compromise and is able to produce good-quality diamond films on substrates as large as 65 mm in diameter with a fast growth rate and at a low cost. Therefore, we chose the direct current CVD technique, operated in gas recycling mode, to prepare freestanding diamond films.^[21–23] Three groups of films were deposited using variations in substrate temperature, methane concentration, and film thickness:

Group I: Variation of substrate temperature: Substrates were kept at three different temperatures, 800, 900, and 1000 °C (± 20 °C), during diamond deposition. The substrate temperature was measured in real time by an infrared thermometer. The methane concentration in the hydrogen feeding flow had a concentration of 1%. The resulting film thickness varied around 150 μm . In the following, the three samples are referred to as 800 °C–1% CH_4/H_2 –150 μm , 900 °C–1% CH_4/H_2 –190 μm , and 1000 °C–1% CH_4/H_2 –140 μm , respectively.

[*] Dr. T. Liu, Prof. D. Raabe, Dr. S. Zaefferer
Max-Planck-Institut für Eisenforschung
Abteilung Mikrostrukturphysik und Umformtechnik
40237 Düsseldorf (Germany)
E-mail: liu@mpie.de; d.raabe@mpie.de
Prof. W. Mao
Department of Materials
University of Science and Technology Beijing
100083 Beijing (P. R. China)

DOI: 10.1002/adfm.200901231

Group II: Variation of methane concentration: The methane concentration in the hydrogen feed flow was varied to three different concentrations, 0.6%, 1%, and 1.5%. The substrate temperature was 1000 °C (± 20 °C). The film thicknesses varied around 250 μm . The three types of samples are referred to as 0.6% CH_4/H_2 –1000 °C–230 μm , 1% CH_4/H_2 –1000 °C–240 μm , and 1.5% CH_4/H_2 –1000 °C–260 μm , respectively.

Group III: Variation of film thickness: Films were deposited with a thickness of 140 and 280 μm . The substrate temperature was 1000 °C (± 20 °C). The methane concentration in the hydrogen feed flow had a concentration of 1%. The two types of samples are referred to as 140 μm –1% CH_4/H_2 –1000 °C and 280 μm –1% CH_4/H_2 –1000 °C, respectively.

We chose molybdenum as the substrate material because the very high and concentrated energy density produced by the direct current arc jet causes the cracking of some other substrate materials, e.g., silicon. Since the roughness of the substrate supports nucleation, the substrates were abraded using diamond powder with an average grain diameter of approximately 10 μm , and subsequently cleaned using ultrasonic waves in order to avoid the remains of the diamond particles.^[24,25] For each sample we studied the free growth surface, the nucleation surface (interface to substrate), and the cross-section (Fig. 1). In order to obtain excellent Kikuchi patterns, the cross-sections were cut using a laser, and then sputtered by Ar ions. The growth and nucleation surfaces were ground using a diamond paste, and then sputtered. Characterization was conducted using scanning electron microscopy (SEM) and HR-EBSD (1 μm step size).

3. Results

3.1. Microstructure

Figure 2a shows the growth surfaces. The microstructures of group I samples show a weak dependence on substrate temperature. The SEM images show faceted grains. Group II samples show that the surface edges of the crystals become less sharp with increasing methane concentration. The grains are composed of irregular facets. Even at a 1.5% methane concentration the morphology shows non-faceted diamond grains. Group III samples reveal that the grain shapes vary only slightly with film thickness. Figure 2b shows as an example specific crystallographic

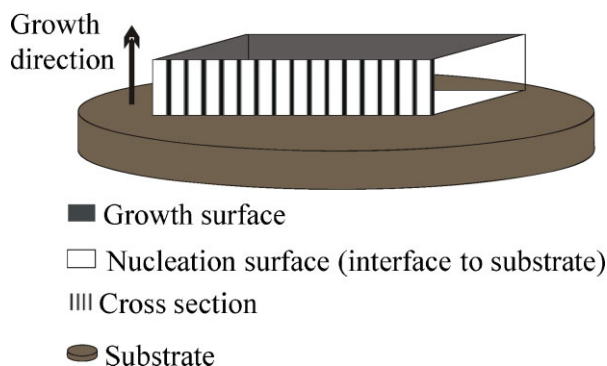


Figure 1. Schematic drawing of the three sample sections studied.

planes in sample 800 °C–1% CH_4/H_2 –150 μm and 140 μm –1% CH_4/H_2 –1000 °C at higher resolution.

3.2. Crystallographic Texture

3.2.1. Orientation Mapping of the Cross-Section

Figures 3–5a show the cross-sections in terms of EBSD maps. The bottom of the maps is the substrate interface and the top is the free surface. The crystal size increases with film thickness. The large grains have a columnar shape in the growth direction and mostly belong to a $\langle 101 \rangle$ texture fiber in the growth direction (Figs 3–5c). The large grains have a homogeneous in-grain texture and often extend from the interface to the free surface. In addition to these large grains, clusters of much smaller grains with non-columnar shape occur (Fig. 4a(γ)). The clusters are often oriented close to the $\langle 001 \rangle$ and $\langle 112 \rangle$ axes (Figs 3–5a,b,c).

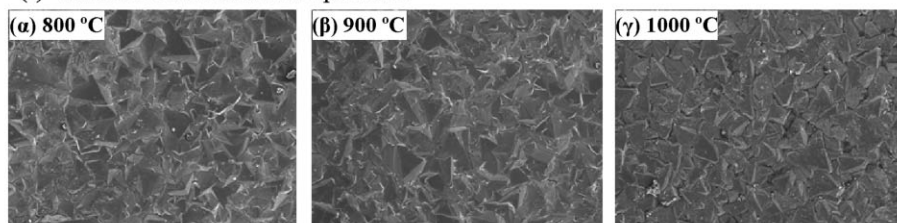
3.2.2. Orientation Mapping of the Nucleation and Growth Surface

Sample 1000 °C–1% CH_4/H_2 –140 μm is given as an example for the microtexture in flat sections both at the nucleation surface (interface to substrate) and at the free growth surface (upper row in Fig. 6). The mean intercept diameter in the cross direction of the (mostly) columnar grains is approximately 2.5 μm in the nucleation interface at the substrate (Fig. 6a) and 12 μm at the free top surface (Fig. 6b).

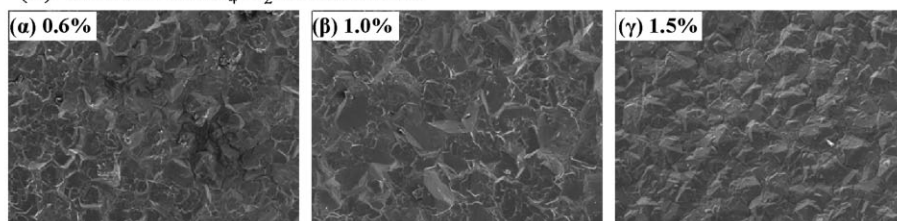
3.3. Grain Boundary Character Distribution

Figures 3–5b and the second row in Figure 6 show the crystallographic character of the grain boundaries both in cross-sections of all samples (Figs 3–5) and for two layers of the sample 1000 °C–1% CH_4/H_2 –140 μm (Fig. 6). The grain boundaries are marked as high angle grain boundaries (black lines) and low angle grain boundaries (gray lines) where the misorientation between two adjacent grains is above 15° and between 2° and 15°, respectively. In addition, special grain boundaries are marked as primary twins (red lines) and secondary twins (green lines) where the misorientation across the interface is described by a $\langle 111 \rangle$ rotation axis and a 58°–62° rotation angle ($\langle 111 \rangle$ 58°–62°) or $\langle 110 \rangle$ 36.9°–40.9° rotation angle, respectively. The cross sections, Figures 3–5b, reveal a large amount of high angle grain boundaries and primary twins in all samples (see Table 1). In particular, group I specimens reveal large fractions of primary twins, namely up to 44% of all high angle grain boundaries when deposited at 800 or 900 °C, respectively. Thicker samples from all three groups reveal some very long primary twin grain boundaries, which are created close to the substrate and prevail up to the free surface. Some of the large grains are associated with such twin boundaries. Secondary twin boundaries also appear occasionally but their fraction does not exceed 4% in any case. Specimens from group I show a much smaller fraction of low angle grain boundaries than samples from groups II and III, Table 1. At the nucleation surface (substrate interface) fewer low angle, primary twin, and secondary twin boundaries appear than close to the free surface (Fig. 6). This observation suggests that non-coherent high angle grain boundaries are dominant at the initial stage of deposition.

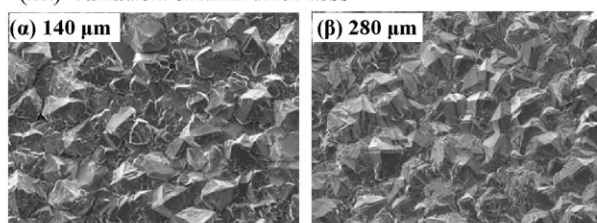
a) (I) Variation of substrate temperature



(II) Variation of CH₄/H₂ concentration



(III) Variation of film thickness



b)

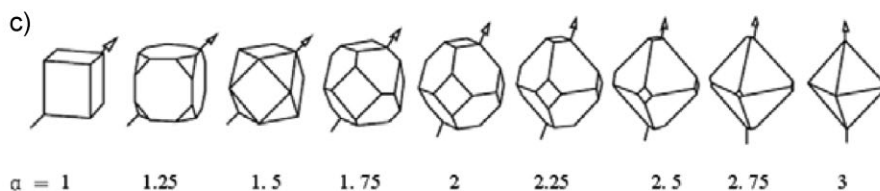
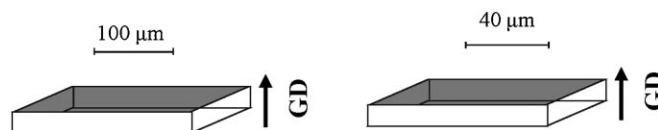
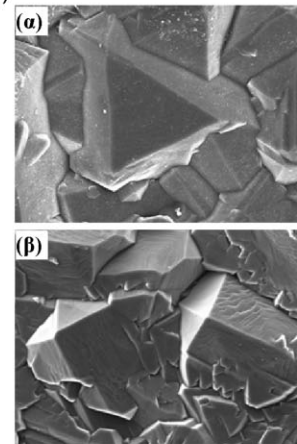


Figure 2. a) Grain shapes and morphologies for different substrate temperatures (group I), different CH₄/H₂ concentrations (group II), and different film thickness (group III). b) Grains in sample 800 °C–1% CH₄/H₂–150 μm (left) and in sample 140 μm–1% CH₄/H₂–1000 °C (right). c) External surface of diamond grains as a function of the facet growth velocity ratio, $\alpha = \sqrt{3}V_{100}/V_{111}$, where V indicates the growth velocity. α increases from left ($\alpha = 1$) to right ($\alpha = 3$) [27].

3.4. Texture Analysis by use of the Orientation Distribution Function (ODF)

The EBSD data presented above were used to calculate the corresponding orientation distribution functions (ODFs). The crystal structure is the diamond (A4) lattice and the sample symmetry was assumed to be triclinic owing to the asymmetry of the deposition process. Figures 7a,b show two types of ODF sections for the EBSD data measured in the cross sections (Figs 3–5), namely, for $\varphi_2 = 45^\circ$ and 15° , where φ_1 and Φ are varied in the range of 0° – 180° . Figure 7c shows the $\varphi_2 = 45^\circ$ sections for the two flat sections.

The $\varphi_2 = 45^\circ$ sections, Figure 7a, show in part fiber type textures, for instance for samples 900 °C–1% CH₄/H₂–190 μm (group I); 1.5% CH₄/H₂–1000 °C–260 μm (group II and particularly pronounced, for 280 μm–1% CH₄/H₂–1000 °C (group III).

Figure 7b shows a {148} texture fiber in the $\varphi_2 = 15^\circ$ section, particularly for samples 800 °C–1% CH₄/H₂–150 μm (group I)

and 280 μm–1% CH₄/H₂–1000 °C (group III). This texture fiber allows one to identify orientations that stem from secondary twinning with respect to the texture components on the {001} fiber texture. Figure 7c shows the orientation density of sample 1000 °C–1% CH₄/H₂–140 μm, which is very weak both in the nucleation (interface) zone and in the growth surface corresponding to the data obtained from the cross sections.

4. Discussion

4.1. Microstructure and Grain Growth Analysis

4.1.1. Microstructure and Surface Appearance

The shape of freely growing diamond crystals is determined by the growth rates of the {001} facets, V_{100} , and {111} facets, V_{111} , i.e.,

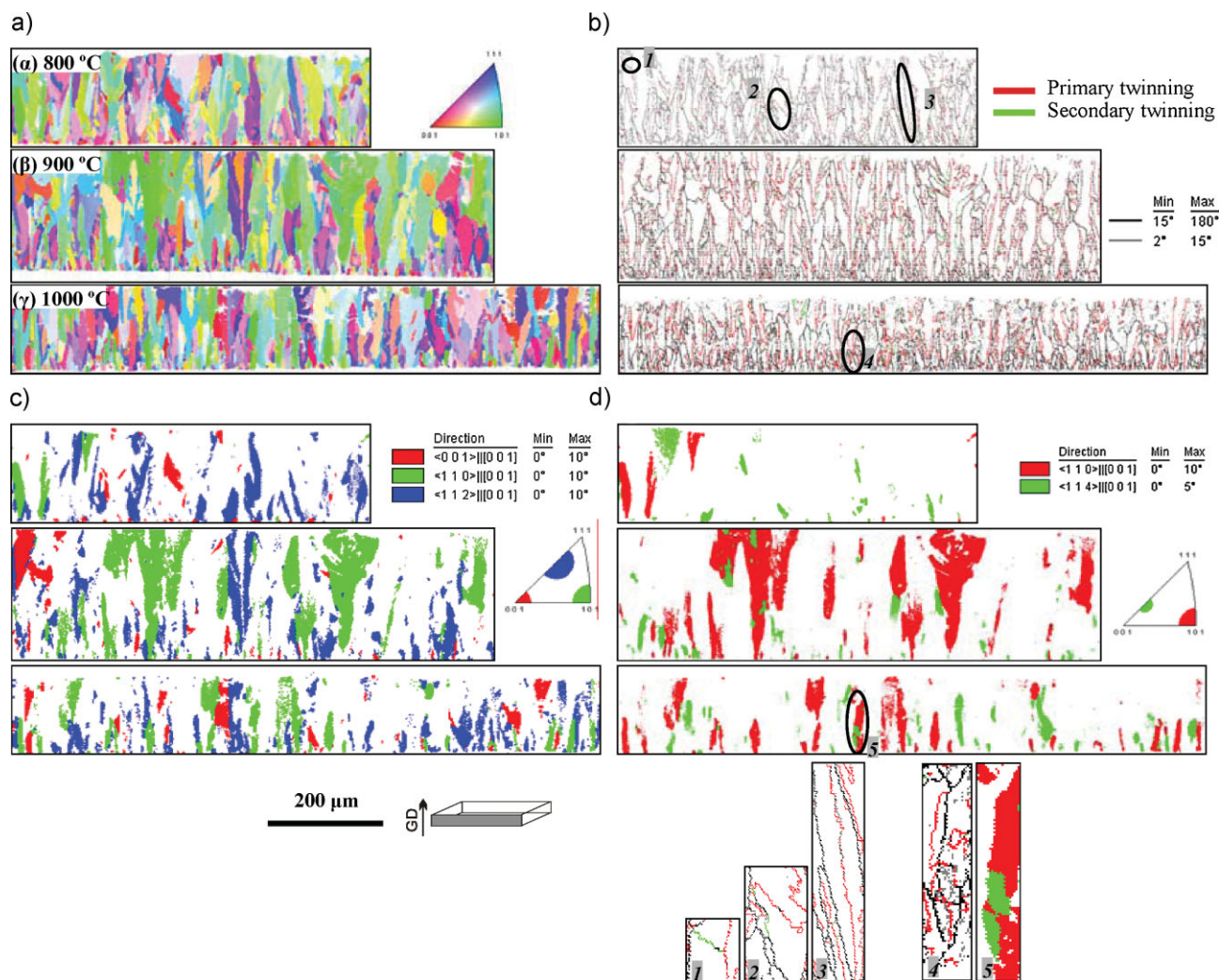


Figure 3. a) Orientation and b) grain boundary maps for different substrate temperatures (cross section view). c) and d) Variations in microtexture presented in terms of certain texture fibers for these three samples. Orientation maps are color coded for the crystal direction parallel to the growth direction.

$\alpha = \sqrt{3} V_{100} / V_{111}$, Figure 2c.^[15,26,27] The arrows in Figure 2c indicate the directions with the highest growth rates. Because of this free growth selection, low-index planes such as {111} and {001} frequently occur at the free surface of the CVD diamond films. The Miller indices of the planes that are visible at the free surface, as well as the corresponding grain orientations, can be understood in terms of the external morphology of the surface grains. For instance, Figure 2a-III-β shows a large amount of {110}-oriented grains that reveal a shape in agreement with the third idiomorphic crystal shape in Figure 2c. This observation indicates that the growth ratio α was in this case close to 1.5. The alignment of the surface polyhedra also allows the estimation that a large fraction of the surface grains has a crystallographic orientation close to a {110} texture fiber, e.g., sample 280 μm–1% CH₄/H₂–1000 °C. Particularly, Figure 2b-α shows a perfect {111} plane, where the growth ratio α was equal to 1.35, i.e., a ratio between the second and the third idiomorphic crystal shape in Figure 2c.^[22] Figure 2b-β shows for sample 140 μm–1% CH₄/H₂–1000 °C two grains that are tilted against the ideal {110} texture, which leads to a

tilted form of the third idiomorphic crystal shape in Figure 2c, $\alpha = 1.5$.

4.1.2. Van der Drift Growth Selection Mechanism

The growth process during CVD deposition can be discussed in terms of a Van der Drift growth selection mechanism,^[28] in which the nucleation stage is characterized by randomly orientated nuclei that grow freely and uniformly according to the growth rate ratio discussed above prior to impingement. The probability of nuclei to prevail is maximal when their fastest growing crystallographic direction is perpendicular to the substrate. These nuclei overgrow less favorably oriented ones, which results in a corresponding crystallographic texture.^[15]

Figures 3–5 reveal the actual growth microstructure formed during the deposition process. For example, a comparison of the nucleation surface with the growth surface in Figure 6 clearly indicates the sharp increase of the grain size by a factor of 5. However, the grain orientations are relatively random both in the

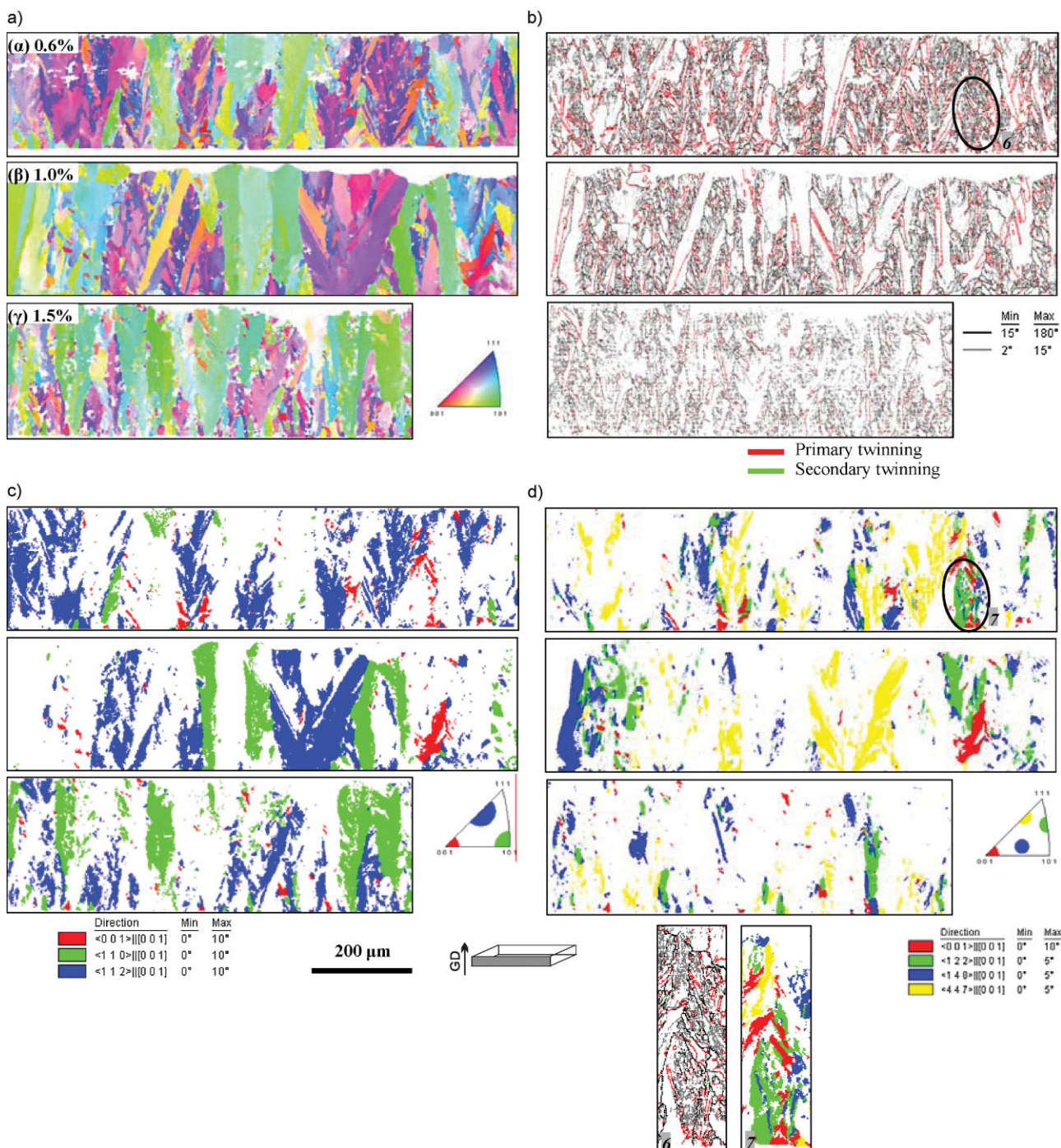


Figure 4. a) Orientation and b) grain boundary maps for different CH_4/H_2 concentrations (cross section view). c) and d) Variations in microtexture presented in terms of certain texture fibers for these three samples. Orientation maps are color coded for the crystal direction parallel to the growth direction.

nucleation zone close to the substrate interface and also at the free growth surface. This can be explained in terms of the cross sections shown in Figures 3–5 that demonstrate that the film growth was frequently interrupted by growth defects, mainly growth twins.

4.1.2.1. Atomistic Growth Models

The growth process can also be discussed in terms of atomistic mechanisms. CVD diamond films are prepared by deposition of carbon atoms after dehydrogenization of activated C_xH_y radicals

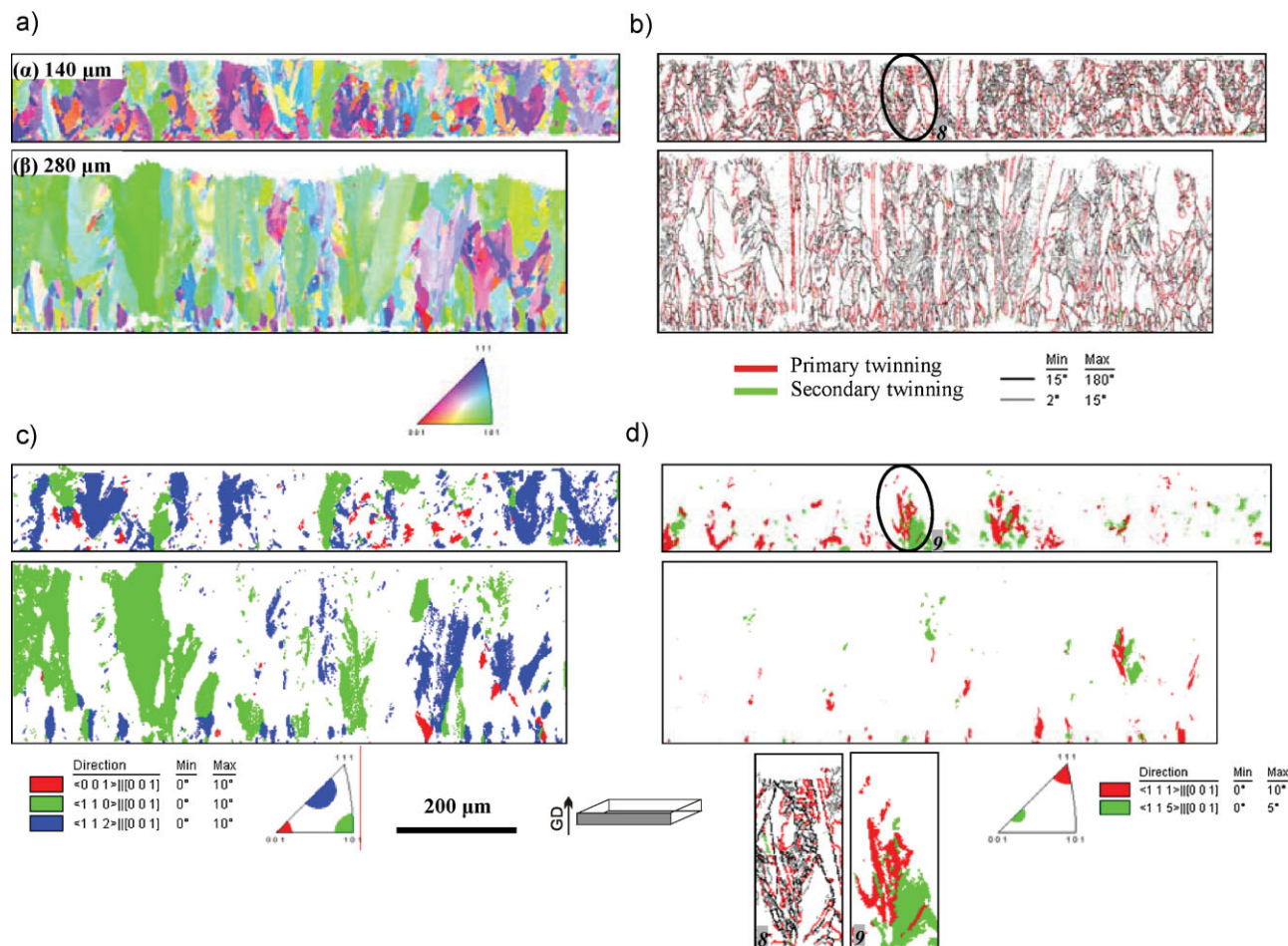


Figure 5. a) Orientation and b) grain boundary maps for different film thickness (cross section view). c) and d) Variations in microtexture presented in terms of certain texture fibers for these two samples. Orientation maps are color coded for the crystal direction parallel to the growth direction.

adsorbed onto a substrate. Single carbon atom (C_1) and double carbon atom (C_2) mechanisms are of main relevance in that context. According to the CVD diamond growth theory and the models developed by Goodwin and Butler,^[29] the C_1 system (C through CH_4) complies with the bimolecular hydrogen shift reactions: $CH_m + H \leftrightarrow CH_{m-1} + H_2$ ($m = 1-4$). According to this reaction sequence, methane molecules, which offer four potential covalent bonds, are sequentially decomposed into activated radicals with a different number of free bonds, i.e., CH_4 , CH_3 , CH_2 , and CH_1 , to C. The sequence and kinetics of these partial molecular processes depend on the deposition atmosphere and on the process parameters (Fig. 8a).^[3] During the deposition process, according to the C_1 mechanism, carbon atoms can be added to the $\{111\}$, $\{001\}$, or $\{110\}$ surfaces.

Based on this molecular decomposition sequence Tsuda et al. proposed the following methyl mechanism: The diamond $\{111\}$ surface is first fully covered by methyl groups, three neighboring methyl groups are then bound spontaneously in one step by the single attack of a methyl cation.^[30] The epitaxial growth of the $\{111\}$ plane then occurs by repeating this reaction chain. Goodwin and Butler objected to this mechanism that involved the addition to the $\{111\}$ surface because of the very low concentration of ionized species in the thermal environment.^[29] In addition, Valone

calculated the energetics of bonding three methyl groups in adjacent positions on the $\{111\}$ surface.^[31] He observed that this process is energetically unstable because of the severe steric constraints between the adjacent groups. Therefore, the $\{111\}$ -surface deposition mechanism proposed by Tsuda et al. does not seem to be free of contradictions at first view.^[30] However, the experimental observations suggest that it cannot be completely ruled out. For example, a perfect $\{111\}$ plane is observed in Figure 2b-α. These types of $\{111\}$ planes have also been observed by other groups.^[22] The experimental observation of diamond growth along the $\langle 111 \rangle$ direction implies the existence of an addition mechanism of carbon atoms to the $\{111\}$ surface. Furthermore, growth along the $\langle 111 \rangle$ direction can only be fulfilled through the repeated deposition of three carbon atoms with at least one dangling bond (i.e., CH_3 , CH_2 , CH_1 , or C) and one carbon atom with at least three dangling bonds (i.e., CH_1 or C). As for the concentration limitation of ionized species, it is hard to define the exact value under which three neighboring methyl groups cannot be bound spontaneously within one step by the single attack of a methyl cation. The semi-empirical methods that Valone employed to calculate the energetics of bonding three methyl groups at adjacent positions were conducted under simplified conditions.^[31] This means that more complex deposition environments and

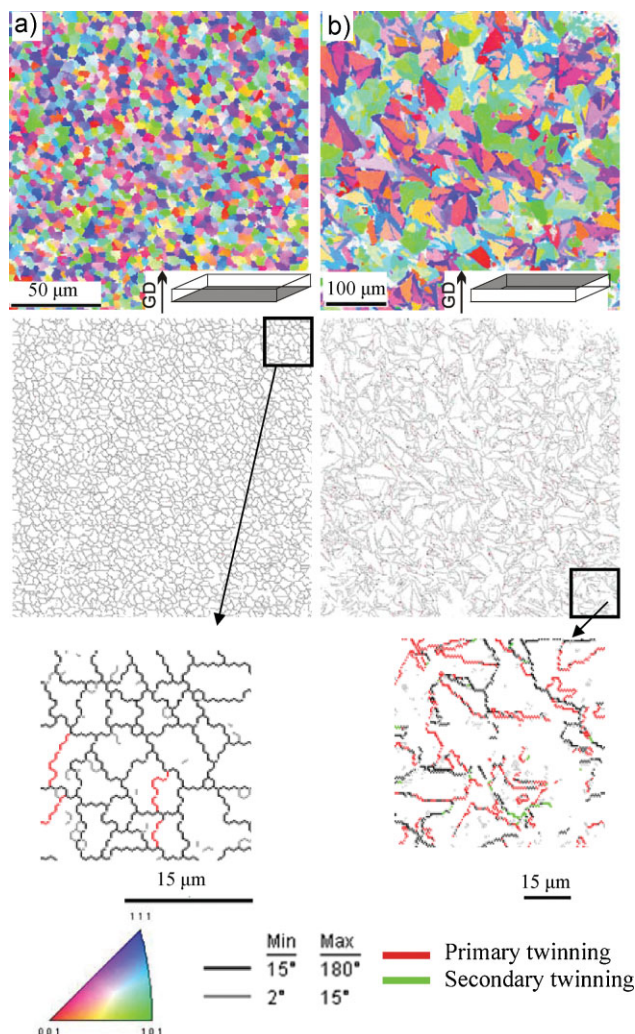


Figure 6. Orientation and grain boundary maps of a) nucleation surface (interface to substrate) and b) free growth surface of sample 1000 °C–1% CH₄/H₂–140 μm (color coded for the crystal direction parallel to the growth direction).

sequences could not be considered. From the above considerations, we conclude that the growth mechanism suggested by Tsuda might be a plausible one in the present case. In addition, it must be considered that diamond growth is a metastable and kinetics-

driven process. It cannot be reduced to the role of an energy barrier that is required to bring three methyl groups at the same time into a nearest-neighbor configuration.

Harris suggested an alternative approach to explain the crystallographic surface orientation dependence of diamond film growth from methyl radicals.^[32] In his approach he used the BCN 9-carbon model compound (C₉H₄, bicyclo[3.3.1]nonane) to describe a proposed mechanism for homoepitaxial growth of diamond on a hydrogenated, electrically neutral (100) surface. Harris estimated enthalpy and entropy changes for each step in this process. In this approach the addition of carbon to the (100) surfaces would be simpler than for (111) or (110) surfaces.

Garrison et al. proposed a low-barrier mechanism: According to their approach a dimer is first opened by abstraction of a surface hydrogen, then by addition of CH₃ followed by abstraction of a methyl hydrogen, and finally by a β-scission reaction which leads to a methyldene intermediate and a radical site.^[33]

In terms of the arguments given above, we propose that the deposition on {111} planes is assumed to work via CH₁ (or C with at least three free bonds) and CH₃ (or CH₂, CH₁, and C with at least one free bond) molecules (Figs 8b,c). The carbon atoms can then deposit along the <111> direction. Growth of {001} planes requires two CH₂ (or CH₁ and C with at least two free bonds) molecules (Figs 8d,e). Likewise, the carbon atoms can laterally occupy the substrate and stack along the <100> direction. In either case, the deposition velocity is proportional to the methane concentration and to the substrate temperature.^[34] Based on the decomposition sequence of methane, the bonding of CH₂–CH₂ occurs before that of CH₃–CH₁, which leads to a kinetic advantage of deposition on {001} planes over that on {111} planes. Another theoretical reason for preferential growth of diamond on {001} facets rather than on {111} facets is the fact that {001} planes were reported to have a lower probability for defect incorporation and twin formation than the {111} facets.^[35]

4.1.2.2. Twinning During Growth

The discussion above was based on the sp³ hybridization of the bonds in CH₄. Real deposition and growth processes in diamond, however, also involve Σ3 primary twinning and a minor fraction of Σ9 secondary twinning. Primary twinning can be understood in terms of the deposition model proposed in Figures 8b,c. At the atomic scale, primary twinning has a low defect energy. In real processes primary twinning is usually observed to increase during ongoing diamond deposition. 60°/⟨111⟩ primary twinning is

Table 1. Grain boundary fractions of each type in the three groups of samples.

Samples		Grain boundary fraction [%]			
		High angle grain boundaries	Low angle grain boundaries	Primary twinning	Secondary twinning
Group I	800 °C–1% CH ₄ /H ₂ –150 μm	95	5	45.1	3.6
	900 °C–1% CH ₄ /H ₂ –190 μm	93	7	44.3	3.4
	1000 °C–1% CH ₄ /H ₂ –140 μm	71.9	28.1	25.9	1.6
Group II	0.6% CH ₄ /H ₂ –1000 °C–230 μm	52	48	23.3	0.4
	1% CH ₄ /H ₂ –1000 °C–240 μm	43.9	56.1	17.4	0.3
	1.5% CH ₄ /H ₂ –1000 °C–260 μm	51.8	48.2	18.5	0.3
Group III	140 μm–1% CH ₄ /H ₂ –1000 °C	59.2	40.8	23.9	0.8
	280 μm–1% CH ₄ /H ₂ –1000 °C	52.9	47.2	22.3	0.6

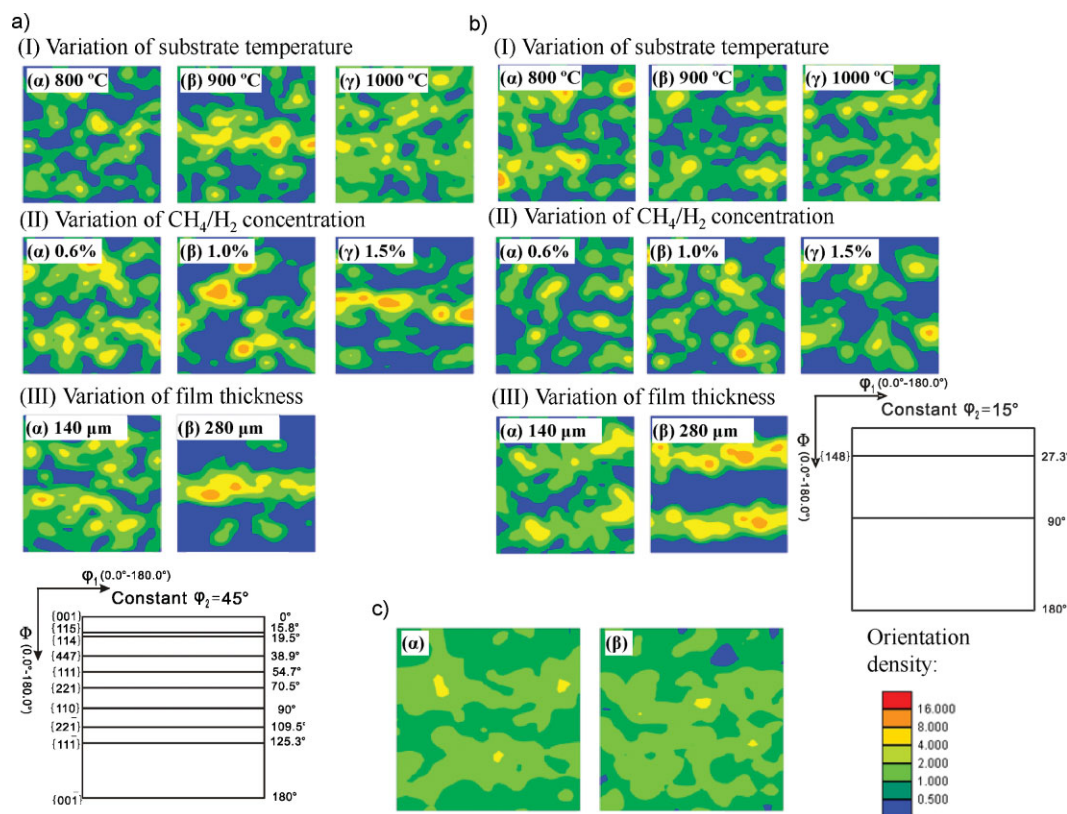


Figure 7. ODF sections at a) $\varphi_2 = 45^\circ$ and b) $\varphi_2 = 15^\circ$ on the basis of the EBSD data obtained from the cross-sections for different: I) substrate temperatures, II) CH_4/H_2 concentrations, and III) film thicknesses. c) ODF section of $\varphi_2 = 45^\circ$ of α) nucleation and β) growth surface of the sample 1000°C –1% CH_4/H_2 –140 μm .

associated with a very small interface energy since the nearest neighbor configuration is the same as for the regular lattice (coherent interface structure). Figure 8f shows the formation of $\Sigma 3$ twins on $\{111\}$ planes, in which the CH_3 radical is geometrically rotated 60° about the $\langle 111 \rangle$ axis on the B layer when compared with the configuration shown in Figure 8b. The stacking sequence becomes then twinned from $\dots\text{ABCABC}\dots$ to $\dots\text{CABAC}\dots$, where the B layer is the twinning plane.

In terms of the twinning model, the $\{001\}$ plane is transformed into the $\{221\}$ plane after twinning. This plane is then further transformed into the $\{148\}$ or $\{447\}$ plane after repeated twinning (secondary twinning). Similarly, the $\{110\}$ and $\{111\}$ planes are transformed during primary twinning into the $\{114\}$ and $\{115\}$ planes, respectively. According to Steeds et al.^[36] secondary twins form through the twinning of primary twins and not by direct $\Sigma 9$ transformation relative to the parent phase (Fig. 8g). Such configurations are marked by Position 1 in Figure 3b- α (see Table 2).

4.2. Microtexture Analysis

The formation of fiber textures is a natural consequence during polycrystalline film growth according to the Van der Drift growth selection.^[28] Our current EBSD results agree well with earlier XRD texture measurements.^[15,16,20]

In this study we particularly analyze the $\langle 001 \rangle$, $\langle 110 \rangle$, and $\langle 111 \rangle$ texture fibers including their primary twin components. For the analysis of these textures fiber components we consider a 10° orientation scatter. In the case of their twinning components 5° is used as the scatter width to avoid overlap with neighboring components (Figs 3–5d).

The EBSD data reveal that the growth directions can strongly change when twinning occurs (Figs 3–5, positions 4–9). Positions 4 and 5 show initial growth in the $\langle 110 \rangle$ direction, subsequent primary twinning into $\langle 114 \rangle$, and back transformation to $\langle 110 \rangle$ by twinning. The evolution of growth in the $\langle 001 \rangle$ direction is more complicated as indicated by positions 6 and 7. It proceeds from $\langle 001 \rangle$, transforms into $\langle 221 \rangle$ by primary twinning, and then further to $\langle 148 \rangle$ and also back to $\langle 001 \rangle$. Positions 8 and 9 show a twinning relation between the $\{111\}$ - and $\{115\}$ -oriented grains. Repeated twinning increasingly randomizes the texture and leads to small grains (Table 2). Figures 3–5c and Figure 3d show that $\langle 110 \rangle$ oriented grains often grow from the initial surface until the final growth surface, which suggests a growth advantage over the other directions (Fig. 9).

4.2.1. Variation of Substrate Temperature

The fiber texture evolution as a function of substrate temperatures is summarized in Figure 9(I). Apparently, the elevated substrate temperature favors grain growth parallel to the $\langle 001 \rangle$ direction. The $\{110\}$ fiber shows a maximum and the $\{111\}$ fiber a minimum

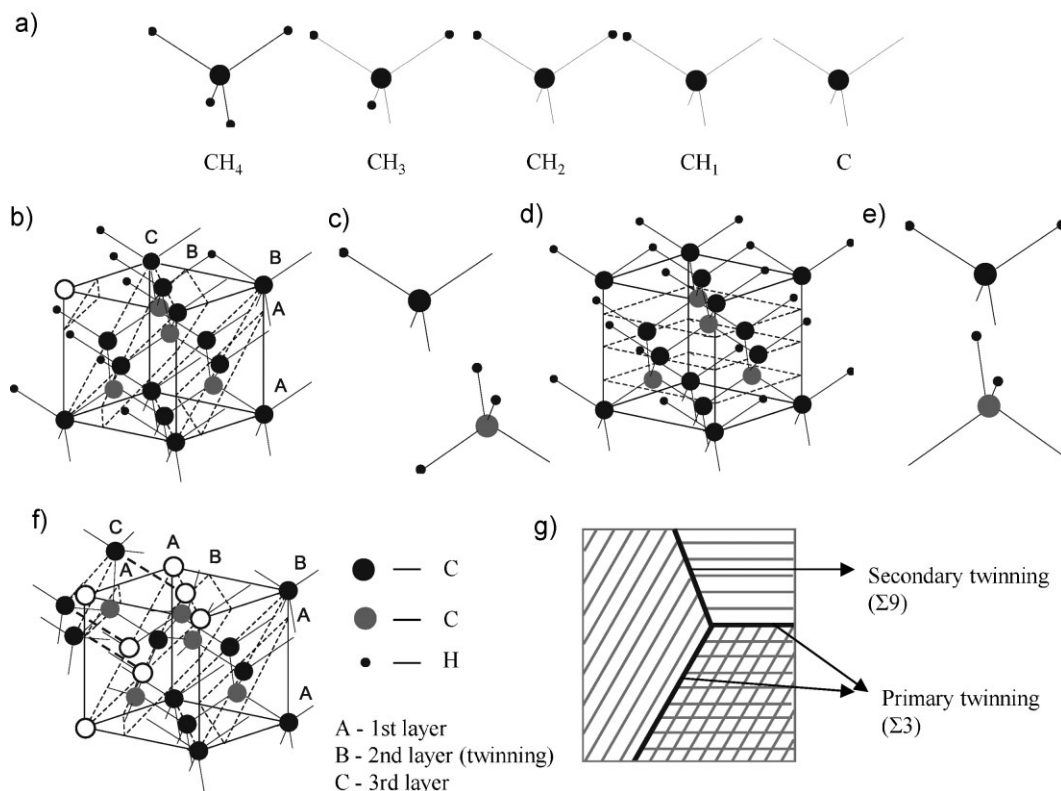


Figure 8. Deposition of diamond grains: a) decomposition sequence of methane molecules, b) deposition process on the $\{111\}$ plane, c) bonding of CH_3 - CH_1 , d) deposition process on the $\{001\}$ plane, e) bonding of CH_2 - CH_2 , f) formation of Σ_3 twinning on $\{111\}$ planes, and g) schematic of the relationship between primary twinning and secondary twinning.

at 900°C . The deposition model shown in Figure 8 is used to explain the results. The methane decomposition rate and diamond deposition rate both increase at higher substrate temperature.^[37,38] The elevated consumption rate of CH_2 impedes further acquisition of CH .^[39] Relatively speaking, CH_1 and C are hardly obtained because of the decomposition sequence. This leads to an increase of the advantage of CH_2 - CH_2 bonds over CH_1 - CH_3 bonds, which accounts for the enhancement of the $\{001\}$ texture fiber. Furthermore, the increase in the deposition rate is supposed to improve the defect density during deposition, which leads to a drop in the stacking fault energy. This leads to easier twinning, which explains an increase of the primary twinning components from the $\{001\}$, $\{110\}$, and $\{111\}$ fibers.

On the other hand, some defects such as H atoms and vacancies are adsorbed onto the growth front, which results in the formation of stacking faults and twins. As the substrate temperature

increases, the adsorbed hydrogen on the growth front is more easily extracted by the hydrogen in the gas phase, which leads to more activated sites. It causes the grains to grow perpendicularly and reduces the crystal defect density. The probability for twinning is decreased with rising substrate temperature.^[40,41] This hypothesis is in agreement with the decrease in the number of twinning components stemming from the $\{001\}$ fiber texture ($\{221\}$, $\{148\}$, and $\{447\}$ components).

The energy of the activated radicals is proportional to the temperature. At low temperatures, this energy readily satisfies the growth condition for the octahedra enveloped by $\{111\}$ planes bearing lower specific surface energy. This leads to the growth of $\{111\}$ planes and to the disappearance of $\{001\}$ planes. As the substrate temperature rises, the kinetic energy of activated radicals increases. This means that the exposure area of the $\{111\}$ planes shrinks and that of the $\{001\}$ planes grows, increasing and

Table 2. Possible transformations by primary twinning and secondary twinning.

Twinning	Rotation angle/axis	Change of lattice plane after primary and secondary twinning
Primary (Σ_3)	$60^\circ/\langle 111 \rangle$	$\{001\} \rightarrow \{221\}$ (1st) $\rightarrow \{148\}$, $\{447\}$, or $\{001\}$ (2nd) $\{110\} \rightarrow \{110\}$ or $\{114\}$ (1st) $\rightarrow \{110\}$, $\{114\}$, $\{778\}$, or $\{4,5,11\}$ (2nd) $\{111\} \rightarrow \{111\}$ or $\{115\}$ (1st) $\rightarrow \{111\}$, $\{115\}$, $\{11,11,1\}$, or $\{5,7,13\}$ (2nd)
Secondary (Σ_9)	$38.9^\circ/\langle 110 \rangle$	$\{001\} \rightarrow \{447\}$ or $\{148\}$ $\{110\} \rightarrow \{110\}$, $\{114\}$, $\{778\}$, or $\{4,5,11\}$ $\{111\} \rightarrow \{115\}$, $\{5,7,13\}$, or $\{11,11,1\}$

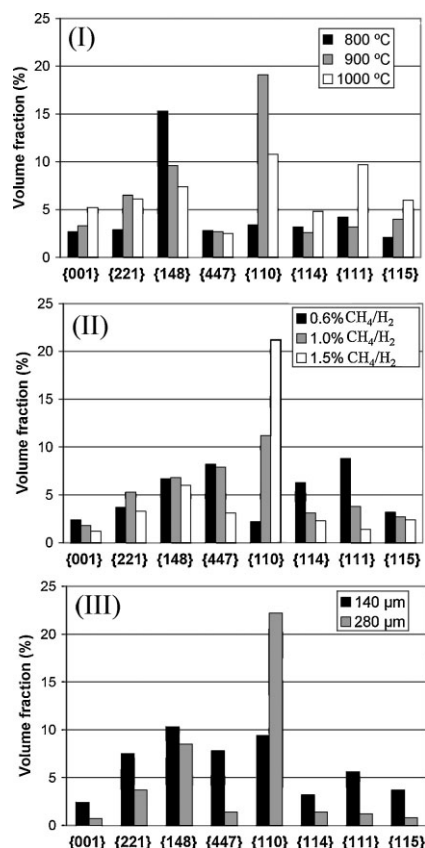


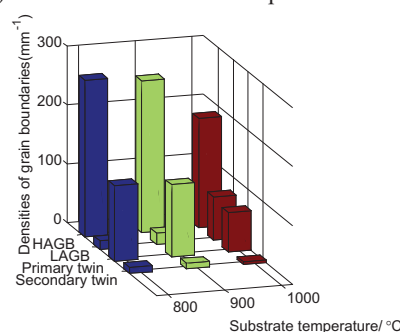
Figure 9. Volume fractions of fiber texture components at different I) substrate temperatures, II) methane concentrations, and III) film thicknesses.

decreasing their normal growth rates, respectively. The external shape is cubo-octahedral at the intermediate stages and finally reaches a cubic shape principally enveloped by {001} planes with a further temperature increase.^[15] Therefore, an elevated temperature level induces the transformation of the fastest crystallographic growth direction from <001>, via <110>, to <111>. This agrees with the decrease of the {001}-group fibers (i.e., {001}, {221}, {148}, and {447} fibers), with the increase of the {110}-group fibers (i.e., {110} and {114} fibers), and the {111}-group fibers (i.e., {111} and {115} fibers), Figure 9(I).

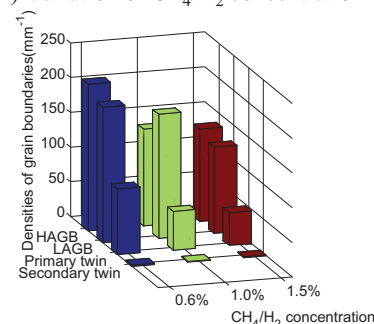
4.2.2. Variation of CH₄/H₂ Concentration

The texture variation as a function of the methane concentration is analyzed in Figure 9(II). The elevated methane concentration promotes grain growth parallel to the crystallographic <110> direction, suppresses growth along <001> and <111> direction, and reduces the density of twinning components generated from the {001}, {110}, and {111} texture fibers. We use the deposition model to explain the observed dependence. We suggest that the rising methane concentration enhances the concentration of activated radicals, which results in an increase of the deposition rate.^[42] The elevated consumption rate of CH₂ prevents a further acquisition of

(I) Variation of substrate temperature



(II) Variation of CH₄/H₂ concentration



(III) Variation of film thickness

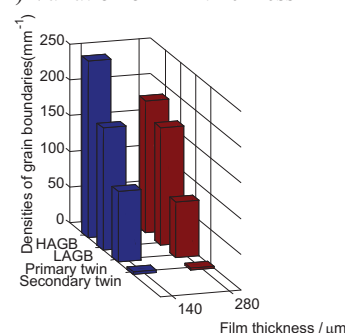


Figure 10. Grain boundary length densities at different I) substrate temperatures, II) CH₄ concentrations, and III) film thicknesses (HAGB: high angle grain boundaries; LAGB: low angle grain boundaries).

CH.^[39] Hence, the deposition on the {001} facets becomes more advantageous over the deposition on {111} facets, which leads to a decrease in the orientation density of the {111} texture fiber, Figure 9(II).

As discussed above, thermodynamic effects may play a role in gas flows with low methane concentration, leading to a higher {111}-plane deposition velocity when compared with {001}, because of a lower surface energy of the {111} planes. This agrees with a low fraction of the {001} texture fiber and with a high fraction of the {111} texture fiber at a methane concentration of 0.6%. The increase of the methane concentration alters the chemical equilibrium in the gas flow mixture and, hence, enhances the collision frequency of the activated radicals with the active surface of the diamond crystals. The film deposition rate is accordingly

increased, which results in a growth advantage of the {001} planes having a lower activation energy than the {111} planes. This agrees with the sharp decrease of the {111} texture fiber from 0.6% to 1.5% methane concentration.

4.2.3. Variation of Film Thickness

The fiber texture variation as a function of film thickness is shown in Figure 9(III). The increase in film thickness weakens grain growth along the {001}, {221}, {148}, {447}, and {111} directions and improves the growth along {110}. According to earlier results^[43–45] diamond films also tend to grow along the {110} direction during deposition, which can be explained in terms of the Van der Drift selection model.^[44] Meakin et al. attributed the rapid growth of the {110} texture to the formation of twins and microtwins.^[46]

4.3. Grain Boundary Analysis

It was observed in diamond that various growth defects appear near high angle grain boundaries while the defect density is low inside individual grains,^[47] e.g., low angle grain boundaries often occur in the vicinity of high angle grain boundaries (Figs 3–5b).

Normally, there are two types of growth relations between parent grains and twins: in series and in paratactic order.^[16] For the case where they grow in series, the parent grains terminate and twins grow out as shown at position 2, Figure 3b. In the case of paratactic growth, parent grains and twins grow out together as shown at position 3. Twinning that occurs primarily in series produces more randomized textures while twinning that occurs in paratactic order does not weaken the prevailing parent texture substantially. In order to compare the variation of various types of grain boundaries, we derived the following statistics from the EBSD data sets: a) We extracted the fractions of the high angle, low angle, primary twin, and secondary twin boundaries from the EBSD data based on the principle described in Section 3.3. b) We analyzed the length densities of the high angle, low angle, primary twin, and secondary twin boundaries. The definition of the length density of the grain boundaries is the total grain boundary length within a unit area. The unit of the interface density is mm^{-1} . The statistical results are illustrated in Table 1 and Figure 10.

4.3.1. Variation of Substrate Temperature

The length densities of the high angle, primary twin, and secondary twin boundaries decrease with rising temperature while that of the low angle grain boundaries rises (Fig. 10(I)). The results reveal that the increasing substrate temperature suppresses planar defects but may intensify the influence of grown-in dislocations that eventually may form low angle grain boundaries. As the temperature goes up, the deposition rate rises. This may lead to a higher grown-in dislocation density. In addition, this could result in a decrease of secondary nucleation during deposition, which implies a decrease of high angle grain boundaries. It is worth noticing that the variation in the volume fraction of the primary and secondary twin boundaries is consistent with that of the high angle grain boundaries, which agrees with the observation that the high angle grain boundaries are the source of lattice defects. According to the results of Sivazlian et al.,^[47] impurity atoms tend

to accumulate at high angle grain boundaries. The higher impurity content reduces the stacking fault energy, which leads to a higher twinning rate.

The volume fraction of the low angle grain boundaries (relative to all internal interfaces) is much higher at 1000 °C than at 800 and 900 °C (Table 1). This effect can be readily explained in terms of the much lower volume fraction of the twin grain boundaries at 1000 °C which form a large portion of the high angle grain boundaries, as shown for all eight samples in Table 1.

4.3.2. Variation of CH_4/H_2 Concentration

The length densities of the high angle, low angle, and primary twin boundaries drop with the increase of the methane concentration (Fig. 10(II)). As the methane concentration increases, the deposition rate rises. Such immediate deposition may lead to a decrease of secondary nucleation during deposition, which implies a decrease of the frequency of high angle grain boundaries. The fraction of secondary twin boundaries is almost independent of the methane concentration.

4.3.3. Variation of Film Thickness

The length densities of high angle, low angle, primary twin, and secondary twin boundaries are reduced as the film thickness increases (Fig. 10(III)). The densities of defects become smaller with increasing film thickness. This means that the deposition process becomes more ordered at the atomistic and microstructural scales with increasing film thickness. In all cases, selective growth is more complicated at the initial stage of deposition than at the later stage. Once the initial nucleation and growth stage is over leading to a front of growing crystals, the remaining growth process is dominated by the high growth rates of those crystals that have an advantageous orientation as discussed above.

5. Summary and Conclusions

EBSD was used to determine microtexture and interfaces in diamond films for different substrate temperature, methane concentration, and film thickness. The results are:

I) Variation of substrate temperature:

The elevated substrate temperature makes $\text{CH}_2\text{--CH}_2$ bonding more advantageous than $\text{CH}_1\text{--CH}_3$ bonding, which leads to a stronger {001} texture fiber. At elevated temperatures the fastest crystallographic growth direction changes from {001}, via {110}, to {111}, due to the lower specific surface energy of the {111} planes.

Increasing substrate temperatures tend to suppress the formation of planar defects. High angle grain boundaries are supposed to be the source of various lattice defects in their vicinity. The impurity accumulation at high angle grain boundaries is assumed to reduce the stacking fault energy locally,^[16] resulting in a higher twinning frequency.

II) Variation of CH_4/H_2 concentration:

Rising methane concentrations lead to a more advantageous deposition on {001} facets and to a decrease of the {111} texture. Growth along {110} is enhanced and twinning is reduced. Thermodynamic effects may play a role in the gas flow at low methane concentration, leading to a lower fraction of the {001}

texture and a higher fraction of {111} at a methane concentration of 0.6%. Kinetic effects prevail with rising methane concentration, leading to a sharp decrease of the {111} texture fiber.

The fraction in the length densities of high angle grain boundaries drops with increasing methane concentration. This may be due to a decrease of secondary nucleation effects induced by immediate deposition.

III) Variation of film thickness:

Diamond tends to grow along the $\langle 110 \rangle$ direction as the films become thicker.

Crystallographic defects are reduced with increasing film thickness.

Acknowledgements

The authors acknowledge the support of International Max Planck Research School for Surface and Interface Engineering in Advanced Materials (IMPRS-SurMat). The authors are grateful to Ms. Katja Angenendt and Ms. Monika Nellessen for the help in sample preparation.

Received: June 27, 2009

Published online: November 19, 2009

- [1] C. A. Klein, *Mater. Res. Bull.* **1992**, 27, 1407.
- [2] P. W. May, *Endeavour Magazine* **1995**, 19, 101.
- [3] M. A. Prelas, G. Popovici, L. K. Bigelow, *Handbook of Industrial Diamonds and Diamond Films*, Marcel Dekker Press, New York **1998**.
- [4] R. E. Clausing, L. L. Horton, J. C. Angus, P. Koidl, *Diamond and Diamond-like Films and Coatings*, Plenum Press, New York **1991**.
- [5] P. Gluche, M. Adamschik, A. Vescan, W. Ebert, F. Szücs, H. J. Fecht, A. Flöter, R. Zachai, E. Kohn, *Diam. Relat. Mater.* **1998**, 7, 779.
- [6] N. Govindaraju, A. Aleksov, X. Li, F. Okuzumi, S. D. Wolter, R. Collazo, J. T. Prater, Z. Sitar, *Appl. Phys. A: Mater. Sci. Process.* **2006**, 85, 331.
- [7] A. K. McCurdy, *Phys. Rev. B* **1982**, 26, 6971.
- [8] A. K. McCurdy, H. J. Maris, C. Elbaum, *Phys. Rev. B* **1970**, 2, 4077.
- [9] Q. F. Su, Y. B. Xia, L. J. Wang, J. M. Liu, W. M. Shi, *Vacuum* **2007**, 81, 644.
- [10] K. Fabisiak, A. Banaszak, M. Kaczmarek, M. Kozanecki, *Cryst. Res. Technol.* **2006**, 41, 535.
- [11] Y. Avigal, O. Glozman, I. Etsion, G. Halperin, A. Hoffman, *Diam. Relat. Mater.* **1997**, 6, 381.
- [12] P. Goudeau, L. Vandenbulcke, C. Met, M. I. De Barros, P. Andreazza, D. Thiaudiere, M. Gailhanouf, *Surf. Coat. Technol.* **2005**, 200, 170.
- [13] A. Schade, S. M. Rosiwal, R. F. Singer, *Diam. Relat. Mater.* **2006**, 15, 1682.
- [14] F. J. Himpsel, J. A. Knapp, J. A. VanVechten, D. E. Eastman, *Phys. Rev. B* **1979**, 20, 624.
- [15] C. Wild, P. Koidl, W. Müller, *Diam. Relat. Mater.* **1993**, 2, 158.
- [16] W. Mao, H. Zhu, L. Chen, H. Feng, F. Lü, *Mater. Sci. Technol.* **2005**, 21, 1383.
- [17] S. Delclos, D. Dorignac, F. Philipp, S. Moulin, A. M. Bonnot, *Diam. Relat. Mater.* **1999**, 8, 682.
- [18] L. W. Yin, M. S. Li, J. J. Cui, Y. J. Bai, B. Xu, J. H. Gong, Z. Y. Hao, *Diam. Relat. Mater.* **2002**, 11, 268.
- [19] T. Liu, D. Raabe, S. Zaefferer, *Sci. Technol. Adv. Mater.* **2008**, 9, 035 013-1.
- [20] T. Liu, D. Raabe, *Appl. Phys. Lett.* **2009**, 94, 021 119-1.
- [21] J. V. Busch, J. P. Dismukes, *Diam. Relat. Mater.* **1994**, 3, 295.
- [22] K. Kobashi, *Diamond Films*, Elsevier, The Netherlands **2005**.
- [23] F. X. Lu, W. Z. Tang, T. B. Huang, J. M. Lin, J. H. Song, W. X. Yu, Y. M. Tong, *Diam. Relat. Mater.* **2001**, 10, 1551.
- [24] L. Sumio, A. Yumi, B. Kazuhiro, *Appl. Phys. Lett.* **1990**, 57, 2646.
- [25] E. Anger, A. Giequel, Z. Z. Wang, M. F. Ravet, *Diam. Relat. Mater.* **1995**, 4, 759.
- [26] P. Hartman, W. G. Perdok, *Acta Crystallogr.* **1955**, 8, 521.
- [27] P. Smereka, X. Q. Li, G. Russo, D. J. Srolovitz, *Acta Mater.* **2005**, 53, 1191.
- [28] A. van der Drift, *Philips Res. Rep.* **1967**, 22, 267.
- [29] D. G. Goodwin, J. E. Butler, in *Handbook of Industrial Diamonds and Diamond Films* (Eds.: M. A. Prelas, G. Popovici, L. K. Bigelow), Marcel Dekker Press, New York **1998**, chapter 2 (*Theory of Diamond Chemical Vapor Deposition*), pp. 527–582.
- [30] M. Tsuda, M. Nakajima, S. Oikawa, *J. Am. Chem. Soc.* **1986**, 108, 5780.
- [31] S. M. Valone, *Mater. Res. Soc. Symp. Proc.* **1989**, 155, 227.
- [32] S. J. Harris, *Appl. Phys. Lett.* **1990**, 56, 2298.
- [33] B. J. Garrison, E. J. Dawnkaski, D. Srivastava, D. W. Brenner, *Science* **1992**, 255, 835.
- [34] H. Maeda, K. Ohtsubo, M. Irie, N. Ohya, K. Kusakabe, S. Morooka, *J. Mater. Res.* **1995**, 10, 3115.
- [35] A. V. Hetherington, C. J. H. Wort, P. Southworth, *J. Mater. Res.* **1990**, 5, 1591.
- [36] J. W. Steeds, A. Gilmore, K. M. Bussmann, J. E. Butler, P. Koidl, *Diam. Relat. Mater.* **1999**, 8, 996.
- [37] I. Schmidt, C. Benndorf, *Diam. Relat. Mater.* **2001**, 10, 347.
- [38] K. Kobashi, S. Miyauchi, K. Nishimura, K. Kumagai, R. Kato, US Patent 5 358 754, (**1994**).
- [39] H. X. Zhu, W. M. Mao, H. P. Hong, F. X. Lu, I. I. Vlasov, V. G. Ralchenko, A. V. Khomich, *J. Inorg. Mater.* **2007**, 22, 570–576. (in Chinese).
- [40] B. E. Williams, H. S. Kong, J. T. Glass, *J. Mater. Res.* **1990**, 5, 801.
- [41] C. S. Yan, K. Yogesh, M. N. Vohra, *Diam. Relat. Mater.* **1999**, 8, 2022.
- [42] C. J. Chu, R. H. Hauge, J. L. Margrave, M. P. D'Evelyn, *Appl. Phys. Lett.* **1992**, 61, 1393.
- [43] C. J. Tang, A. J. Neves, A. J. S. Fernandes, *Diam. Relat. Mater.* **2003**, 12, 1488.
- [44] C. Wild, N. Herres, P. Koidl, *J. Appl. Phys.* **1990**, 68, 973.
- [45] R. E. Clausing, L. Heatherly, L. L. Horton, E. D. Specht, G. M. Begun, Z. L. Wang, *Diam. Relat. Mater.* **1992**, 1, 411.
- [46] D. Meakin, J. Stoemenos, D. Migliarete, N. A. Economou, *J. Appl. Phys.* **1987**, 61, 5031.
- [47] F. R. Sivazlian, J. T. Glass, B. R. Stoner, *J. Mater. Res.* **1994**, 9, 2487.